

**SUPPLEMENTARY DATA****DRB4 dsRBD1 drives dsRNA recognition in *Arabidopsis thaliana* tasi/siRNA pathway****Sai Chaitanya Chiliveri<sup>1</sup>, Ramdas Aute<sup>1</sup>, Upasana Rai<sup>1,2</sup> and Mandar V. Deshmukh<sup>1,2,\*</sup>**<sup>1</sup>CSIR-Centre for Cellular and Molecular Biology, Uppal Road, Hyderabad, 500007, INDIA.<sup>2</sup>Academy of Scientific and Innovative Research (AcSIR), CSIR – Centre for Cellular and Molecular Biology, Uppal Road, Hyderabad, 500007, INDIA.\*Corresponding author: Phone: +91-40-2719-2646; email: [mvdesh@ccmb.res.in](mailto:mvdesh@ccmb.res.in)**SUPPLEMENTARY MATERIALS AND METHODS****Cloning, expression and purification**

DRB4 (1-355) (hereafter DRB4) was amplified from pGEX6p-DRB4 containing full length DRB4. The amplified PCR fragment was double digested with restriction enzymes, NdeI and XhoI and ligated into pET-30a using standard molecular biology techniques. The truncated fragments of DRB4; DRB4 (1-153) (hereafter DRB4D1D2), DRB4 (1-75) (hereafter: DRB4D1), DRB4 (80-153) (hereafter: DRB4D2), DRB4 (154-355) (hereafter: DRB4C), DRB4 (294-355) (hereafter: DRB4Cc), DRB4 (72-81 connected to 4-71) (hereafter: DRB4LD1) and DRB4 (72-153) (hereafter: DRB4LD2) were also cloned into pET-30a in a similar way.

Domain swapped construct, DRB4D2D1 was prepared by two-step PCR, wherein the part of linker sequence was introduced to dsRBD1 and dsRBD2 at their N-terminus and C-terminus, respectively and PCR amplified separately. The amplified fragments were annealed with overlapping linker region and PCR amplified to generate DRB4D2D1.

DRB4D1D2 containing native cysteines at 38<sup>th</sup> and 43<sup>rd</sup> residues were mutated to alanine to generate cysteine-less DRB4D1D2. Several constructs with single surface exposed cysteine were generated in DRB4D1D2 at Q8, A24, A69, N85, A102 and M138 amino acid positions. Samples with 25  $\mu$ M concentration (in 50 mM potassium phosphate buffer (pH 7.2), 50 mM NaCl and 50 mM Na<sub>2</sub>SO<sub>4</sub>) were incubated overnight with 5 molar excess (2,2,5,5-tetramethyl-2,5-dihydro-1H-pyrrol-3-yl) methyl methanesulfonylthioate (MTSL) at 4°C. Further, the samples were centrifuged at 10,000 rpm, 4°C for 10 min to remove aggregated protein. Later, samples were washed multiple times to remove unreacted MTSL from the solution and concentrated to 250  $\mu$ M. Diamagnetic samples were prepared by addition of 5 molar excess ascorbic acid to the paramagnetic sample.

Seven active site mutations were created for DRB4D1D2, which includes five double mutants (K6A/Q10A; L56A/K57A; K84A/Q88A; K133A/K134A and H32A/K133A) and two single mutants (H32A and H110A). Likewise, three active site double mutants (L56A/K57A; K133A/K134A and H32A/K133A) were generated for DRB4. Site directed mutagenesis was performed by sequentially mutating the required amino acids to alanine by whole plasmid PCR with primers containing desired nucleotide mismatch.

All constructs followed previously optimized expression and purification conditions established for DRB4D1D2 (1).  $^{15}\text{N}$  labeled samples were prepared by growing bacterial cells in M9 minimal medium containing  $^{15}\text{N}$   $\text{NH}_4\text{Cl}$  as a sole nitrogen source. In addition to  $^{15}\text{N}$   $\text{NH}_4\text{Cl}$ ,  $^{13}\text{C}$  D-glucose was added to the minimal media for preparing U- $^{13}\text{C}$ ,  $^{15}\text{N}$  labeled samples.

DCL4 DUF283 was expressed and purified as described in Qin et al. (2). The resonances in  $^1\text{H}$ - $^{15}\text{N}$  HSQC were matched to the assignments derived from BMRB ID 16534, confirming identical structural fold. [U- $^{15}\text{N}$ ]AtDCL4-DUF283 was concentrated to 200  $\mu\text{M}$  (in 20 mM HEPES (pH 7.2), 100 mM NaCl and 2 mM DTT) and titrated with equimolar concentrations of unlabeled DRB4D1D2.

### Backbone chemical shift assignments of DRB4D2D1, DRB4C and DRB4Cc

Unambiguous backbone chemical shift assignments were obtained using standard triple resonance experiments. The backbone chemical shift assignments of DRB4C were achieved using HNCO, HN(C)N and HNN based experiments (3,4). Nearly 82% of the backbone chemical shifts for residues 154 to 313 could be assigned. This does not include the structured C-terminal region (DRB4Cc) as the resonances for this region are missing due to the enhanced  $\tau_c$  and associated deleterious relaxation effects induced by the long N-terminal unstructured region. Attempts to assign the backbone chemical shifts of DRB4Cc, using classical as well as non-uniform sampling methods, failed due to its extreme unstable nature suggesting the requirement of a partner protein for its stability.

### NMR derived restraints and structure calculation

All NMR spectra were collected at 298K on Bruker Avance II 600MHz or Avance III 700 MHz NMR spectrometer, which are equipped with a triple resonance TCI cryoprobe.

Prior to structure calculation, dihedral angles were obtained from backbone chemical shifts ( $\text{H}^{\text{N}}$ , N,  $\text{H}\alpha$ , C',  $\text{C}\alpha$ ,  $\text{C}\beta$ ) using TALOS+ (5). Based on the intensities of NOE cross peaks, distance restraints were classified into 4 bins: 1.8-3.0Å (strong), 1.8-4.0 Å (medium), 1.8-5.0Å (weak) and 1.8-6.0Å (very weak). For NOEs involving methyl groups, 0.5 Å was added to the existing distance restraints. Using simulated annealing procedure; initial structures were calculated from the dihedral and distance restraints from an extended structure (6). Hydrogen bond restraints,  $\text{H}^{\text{N}} - \text{O}$  and  $\text{N} - \text{O}$  were assigned with 1.8-2.5Å and 1.8-3.5Å, respectively.

$\text{H}^{\text{N}} - \text{H}^{\text{N}}$  distance restraints were derived from a 3D version of 4D  $^1\text{H}$  ( $^{15}\text{N}$ )-HMQC-NOESY- $^{15}\text{N}$  FHSQC ( $\tau_m = 200$  ms) on [U- $^{15}\text{N}$ ] DRB4D1D2. Other distance restraints were obtained from 3D NOESY- $^{15}\text{N}$  HSQC ( $\tau_m = 80$  ms and 120 ms) and 3D NOESY- $^{13}\text{C}$  HSQC ( $\tau_m = 80$  ms and 120 ms), respectively on [U- $^{13}\text{C}$ ,  $^{15}\text{N}$ ] DRB4D1D2, [U- $^{13}\text{C}$ ,  $^{15}\text{N}$ ]DRB4D1 and [U- $^{13}\text{C}$ ,  $^{15}\text{N}$ ]DRB4D2. Residual dipolar couplings were measured using in-phase anti-phase  $^1\text{H}$ - $^{15}\text{N}$  HSQC under isotropic and anisotropic media (7). For obtaining anisotropic environment, [U- $^{13}\text{C}$ ,  $^{15}\text{N}$ ] DRB4D1D2 was externally aligned in 18 mg/mL Pf1 phages. Non-exchangeable protons of DRB4D1D2 were identified from  $^1\text{H}$ - $^{15}\text{N}$  HSQC on [U- $^{15}\text{N}$ ]DRB4D1D2 in 100%  $^2\text{H}_2\text{O}$ .

Initial structures were calculated with all NOEs and dihedral angle information. A square-well penalty function is used for all restraints with following force constants, 50 kcal mol $^{-1}$  Å $^{-2}$ , 200 kcal mol $^{-1}$  rad $^{-2}$ , 1 kcal mol $^{-1}$  Hz $^{-2}$  for NOEs, torsional angles, and RDCs, respectively.

For diamagnetic and paramagnetic samples,  $^1\text{H}$ - $^{15}\text{N}$  HSQCs were recorded under identical conditions. Spectra of diamagnetic and paramagnetic samples were similar to DRB4D1D2, suggesting no change in the overall fold due to cysteine mutations. Intensity ratios of cross-peaks in  $^1\text{H}$ - $^{15}\text{N}$  HSQCs under paramagnetic and diamagnetic spectra were estimated. The theoretical distance,  $r$ , from the paramagnetic center to the amide proton was derived by fitting following equation (Eq. 1) and by varying  $R_2^{\text{sp}}$  and using experimentally derived  $\tau_c$  of 11 ns for DRB4D1D2.

$$r = \left[ \frac{K}{R_2^{\text{sp}}} \left( 4\tau_c + \frac{3\tau_c}{1 + \omega^2\tau_c^2} \right) \right]^{\frac{1}{6}} \quad (1)$$

Average  $^1\text{H}$   $R_2$  rates under diamagnetic conditions were found to be  $55 \text{ s}^{-1}$  from proton linewidths, as described by Battiste et al. (8). Further,  $I_{\text{para}}/I_{\text{dia}}$  was theoretically derived after considering  $t = 11 \text{ ms}$  and by fitting following equation (Eq. 2).

$$\frac{I_{\text{para}}}{I_{\text{dia}}} = \frac{R_2 \exp(-R_2^{\text{sp}}t)}{R_2 + R_2^{\text{sp}}} \quad (2)$$

Further, simulated curves were generated for conversion of intensity ratios into distances and used as ready reckoner to estimate distances for experimentally derived  $I_{\text{para}}/I_{\text{dia}}$  ratios (Supplementary Fig. S12a). Quality of the PRE restraints was calculated using the following equation (Eq. 3).

$$Q^{\text{PRE}} = \sqrt{\frac{\sum (V_{\text{backcalc}} - V_{\text{exp}})^2}{\sum (V_{\text{exp}})^2}} \quad (3)$$

Intradomain PREs were used to calibrate the intensities. The distances derived from PRE were estimated using the method described by Rumpel et al. (9). On an average, it was found that MTSL influenced amide NH crosspeak intensities up to 21 Å. PRE based distance restraints were categorized into three classes. Resonances with intensity ratio above than 0.2 and less than 0.85 ( $0.2 < I_{\text{para}}/I_{\text{dia}} < 0.85$ ), were restrained to 17 Å with an error set to 4Å. Peaks with intensities above 0.85 were restrained to 90 Å as upper bound distance and 16 Å as the lower bound limit. For resonances with intensity ratio less than 0.2, lower and upper bound distances were set to 2.8 Å and 13 Å, respectively.

Once the individual domain structures were obtained, PREs (six sets: Q8C, A24C, A69C, N85C, A102C and M148C) were included in the structure calculations. Final structures were calculated with the incorporation of all NOEs, dihedral angles, six sets of PREs and refined with RDCs. As errors in PREs were up to 4 Å, categorizing the PRE distances into 3 bins did not greatly affect the calculated structures as described earlier (8).

### $^{15}\text{N}$ relaxation dispersion

$^{15}\text{N}$  relaxation dispersion experiments were collected on DRB4D1 and DRB4D2 using relaxation compensated CPMG (RC CPMG) scheme (10). Every relaxation dispersion profile was comprised of 15  $\nu_{\text{CPMG}}$  points (33.3, 66.7, 100, 133.3, 166.7, 200, 233.3, 300, 400, 500, 600, 700, 800, 900 and 1000 Hz)

collected over a constant relaxation time of 30 ms. For error analysis, a pair of duplicate and triplicate points were collected for dsRBD1 and dsRBD2, respectively. NMR spectra were processed using NMRPipe, assignments and peak adjustments were carried out using SPARKY (11,12). Relaxation dispersion data from both fields were fitted simultaneously to fast limit CPMG function (Eq. 4) using CPMGFit (<http://www.palmer.hs.columbia.edu>).

$$R_2(1/\tau_{cp})=R_2+R_{ex} \times (1 -(2 \times \tau/\tau_{cp}) \times \tanh(1/(2 \times \tau/\tau_{cp}))) \quad (4)$$

### RNA preparation

13 bp RNA (sense: 5'-UGA GGU AGU AGA G UU-3') and 20 bp RNA (sense: 5'- UGA GGU AGU AGG UUG UAU AG UU-3') containing 2nt 3' overhang were custom synthesized, desalted, HPLC purified and obtained commercially. 80 bp dsRNA with the sense strand sequence as, 5'-GGG UGC UGU UUC UCG UGU UCG UGU UCG UUU CUCU UCU CUU GUC CUU GUU CUG UUC UCC UUU GUU CGU UCC UGU UCC CCU U-3' was transcribed *in vitro* using T7 RNA polymerase. *In vitro* transcribed product was digested with Turbo DNaseI and RNA was purified by phenol chloroform extraction, followed by ethanol precipitation and gel extraction. Prior to dsRNA assays, equimolar concentrations of sense and antisense RNA were annealed in dsRNA buffer (20 mM HEPES (pH 7.2), 50 mM NaCl and 2 mM DTT) by heating at 95°C for 5 min, followed by flash cooling at 4°C.

### Guanidine Hydrochloride denaturation studies

A series of  $^1\text{H}$ - $^{15}\text{N}$  HSQCs were recorded for [ $^{15}\text{N}$ ] DRB4C (100  $\mu\text{M}$  in 50~mM potassium phosphate buffer (pH 6.5), 50 mM NaCl, 50 mM  $\text{Na}_2\text{SO}_4$  and 2 mM DTT) in 0 M, 2 M, 4 M, 6 M and 8 M concentrations of guanidine hydrochloride (GuHCl) at 25°C.

### Small angle X-ray scattering (SAXS) and structure modeling

SAXS measurements were performed using in-house instrument, S3 Micro (Hecus X-ray systems). Scattering was collected on DRB4D1D2 (in 20 mM sodium phosphate buffer (pH 7.4), 100 mM NaCl and 2 mM DTT) with concentrations ranging from 5 mg/mL to 20 mg/mL and samples were kept 300 mm from the Pilatus 100 K detector. Raw data was processed using FIT2D program (13). Radius of gyration ( $R_g$ ) and  $D_{max}$  were calculated from PRIMUS and GNOM (14,15). Ten low-resolution *ab initio* structures were constructed using DAMMIN and averaged using SUPCOMB and DAMAVER (16,17).

### Analytical ultra centrifugation

Sedimentation velocity (SV) experiment was performed at 40,000 rpm at 20°C on 0.1-1.25 mg/mL concentrations of DRB4C using Beckman Optima XL-I analytical ultracentrifuge. Prior to the measurements, samples were buffer exchanged with 50 mM potassium phosphate buffer (pH 7.2), 100 mM  $\text{Na}_2\text{SO}_4$  and 2 mM DTT. Measurements were collected for every 12 min interval using absorbance optics. Sedimentation coefficient  $S_{20,w}$  and molecular weight of the protein was calculated by fitting the non-linear sedimentation boundary profile with Lamm equation (Eq. 5) using SEDFIT package. The parameters required, like viscosity, partial specific volume, density were obtained from SEDNTERP.

$$\frac{dc}{dt} = \frac{1}{r} \times \frac{d}{dr} \left[ rD \frac{dc}{dr} - s\omega^2 r^2 c \right] \quad (5)$$

## Supplementary table

Table S1: Thermodynamic parameters derived from ITC for binding of DRB4 constructs to dsRNA.

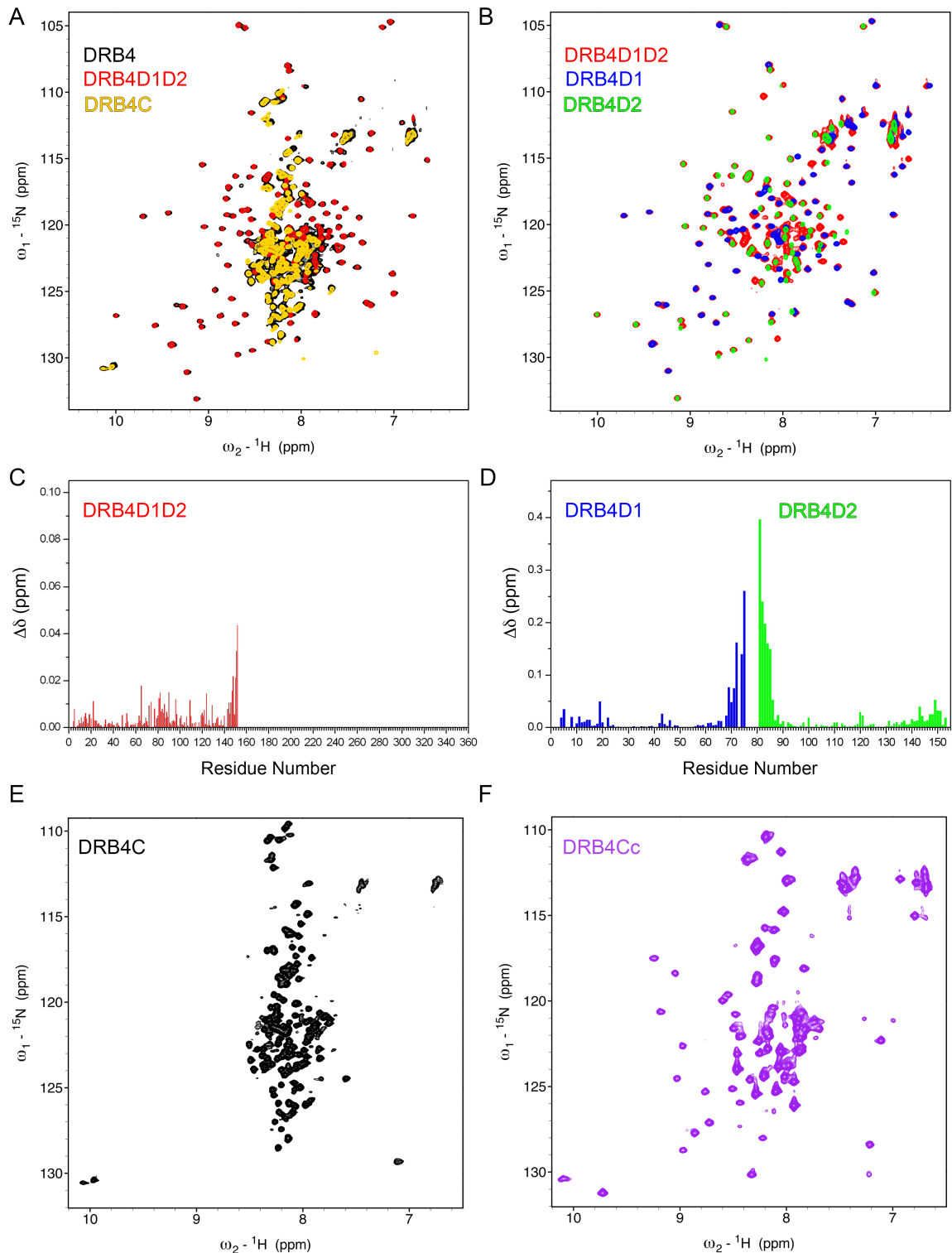
S. No	Construct	$K_d$ ( $\mu$ M)		N	$\Delta H$ (Kcal/mol)	$\Delta S$ (cal/mol/deg)	$\Delta G$ (Kcal/mol)
A. 80 bp dsRNA (RNA in cell and protein in syringe)							
1	DRB4WT	0.12 $\pm$ 0.04		1.9	-7.76	5.06	-9.27
2	DRB4D1D2	0.40 $\pm$ 0.03		2.7	-9.22	-1.79	-8.68
3	DRB4D2D1	4.0 $\pm$ 0.4		2.7	-23.68	-54.6	-7.40
B. 20 bp dsRNA (Protein in cell and RNA in syringe)							
1	DRB4D1D2	Site 1	7.3 $\pm$ 0.6	0.12	-83.56	-257	-6.97
		Site 2	0.2 $\pm$ 0.1	0.23	-10.98	-6.01	-9.18
2	DRB4D2D1	4.5 $\pm$ 0.4		0.35	-45.28	-127	-7.43
3	DRB4D1	Site 1	2.7 $\pm$ 0.7	0.23	-4.01	12.0	-7.58
		Site 2	0.3 $\pm$ 0.2	0.23	2.40	38.0	-8.92
4	DRB4D2	1.0 $\pm$ 0.04		0.25	-69.09	-204	-8.29
5	DRB4C	NB		NB	NB	NB	NB
C. 20 bp dsRNA (RNA in cell and protein in syringe)							
1	DRB4D1D2*	2.4 $\pm$ 0.3		NA	-13.02	-18.0	-7.65
2	DRB4D1*	8.7 $\pm$ 2.8		NA	-10.59	-12.4	-6.89
3	DRB4D2	2.0 $\pm$ 0.1		NA	-20.27	-41.9	-7.78
D. Zn <sup>2+</sup> titration (Protein in cell and ZnCl <sub>2</sub> in syringe)							
1	DRB4D1D2	NB		NB	NB	NB	NB
2.	DRB4C	23.6 $\pm$ 1.8		3.5	-1.88	14.8	-6.29

NA = Not Applicable

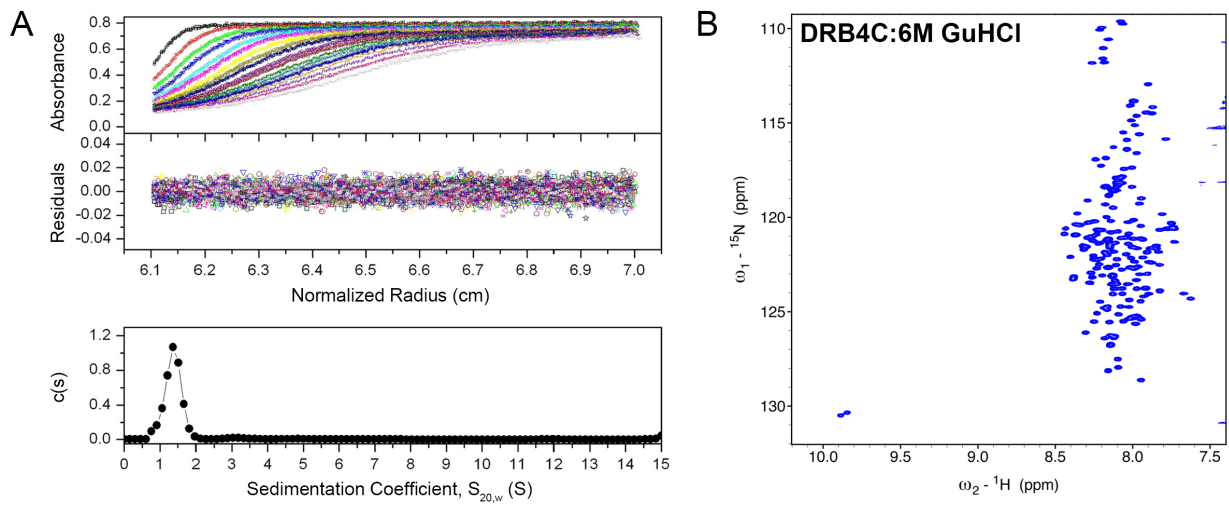
NB = Does not bind

\*a single average confirmation is observed upon titration of these domains into excess dsRNA.

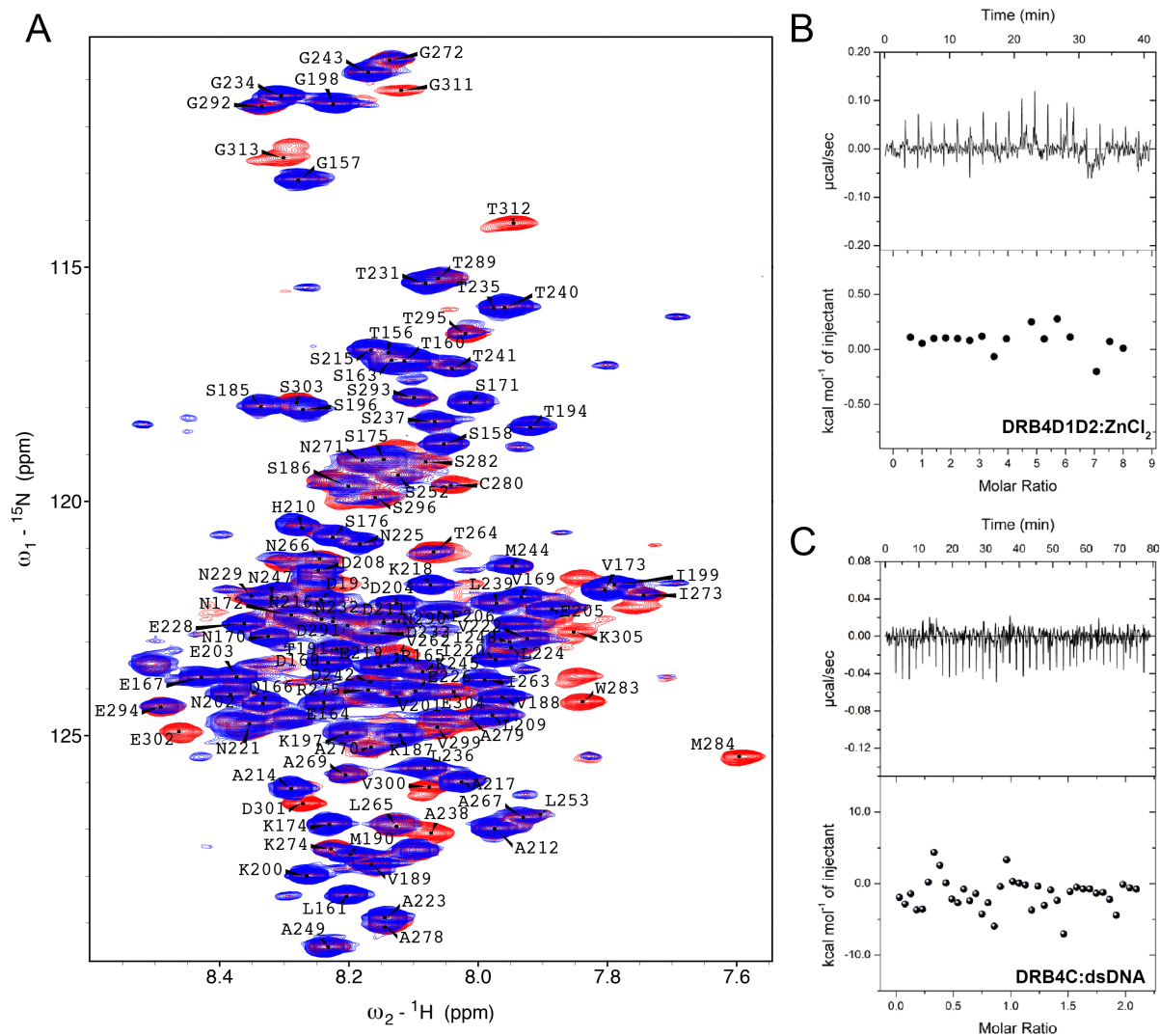
## Supplementary Figures and Legends



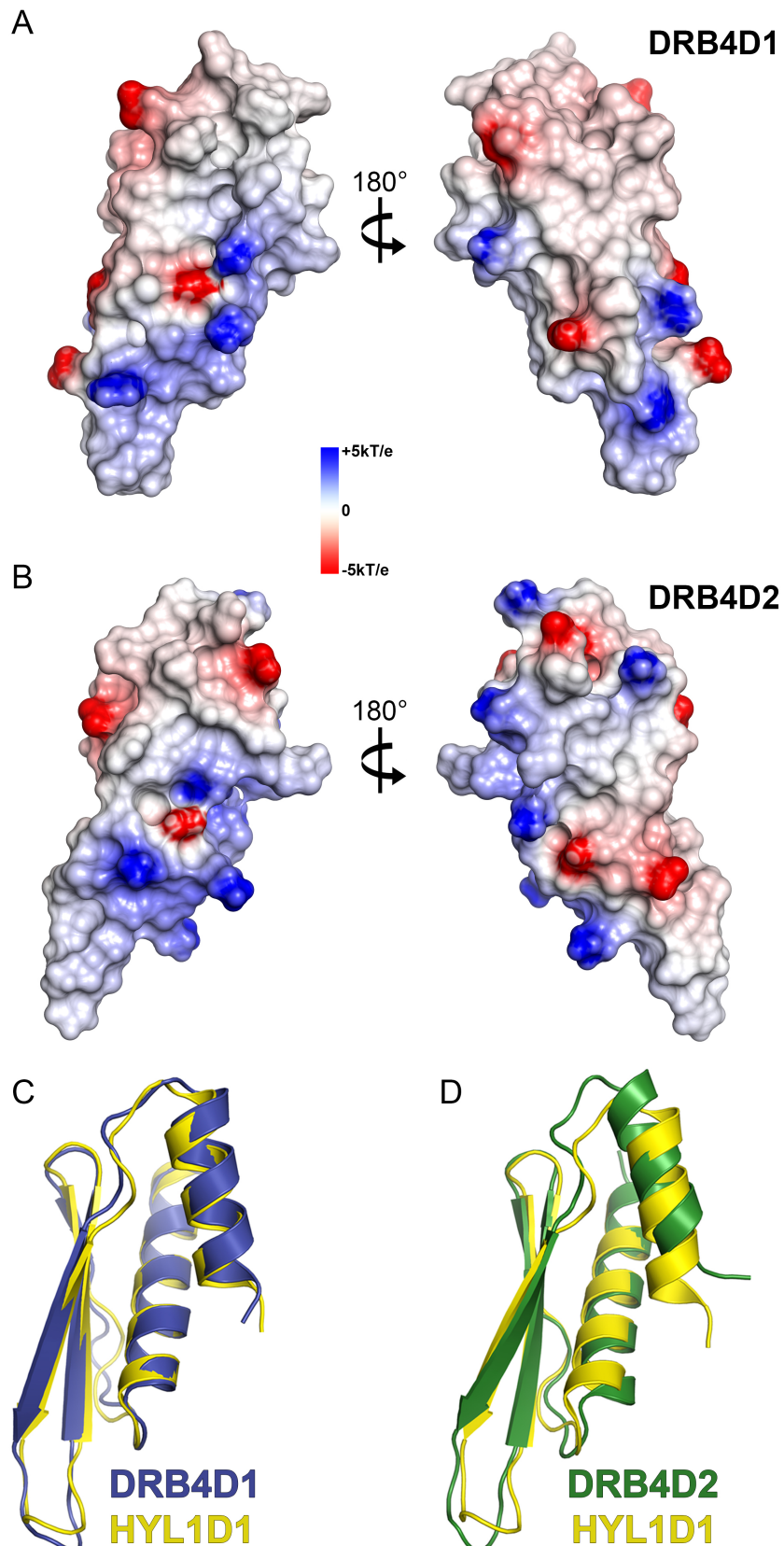
**Supplementary Figure S1.** Fold comparison of individual domains in DRB4. **(A)** Overlay of  $^1\text{H}$ - $^{15}\text{N}$  TROSY-HSQC spectra of DRB4D1D2 (red) and DRB4C (yellow) with DRB4 (black). **(B)**  $^1\text{H}$ - $^{15}\text{N}$  TROSY-HSQC of DRB4D1D2 (red) with DRB4D1 (blue) and DRB4D2 (green). **(C)** Normalized chemical shift changes along residue number indicate chemical shifts of DRB4D1D2 are not significantly influenced by the presence of DRB4C, indicating that they do not interact with each other. **(D)** Normalized chemical shift perturbations as a function of residue number shows that DRB4D1 and DRB4D2 exhibit identical chemical shifts in the absence of the other domain except for the terminal residues. **(E)**  $^1\text{H}$ - $^{15}\text{N}$  TROSY-HSQC spectrum shows narrow spectral dispersion in the proton dimension for DRB4C, indicating its partially folded structure. **(F)** The  $^1\text{H}$ - $^{15}\text{N}$  HSQC spectrum of DRB4Cc is well dispersed suggesting its tertiary fold.



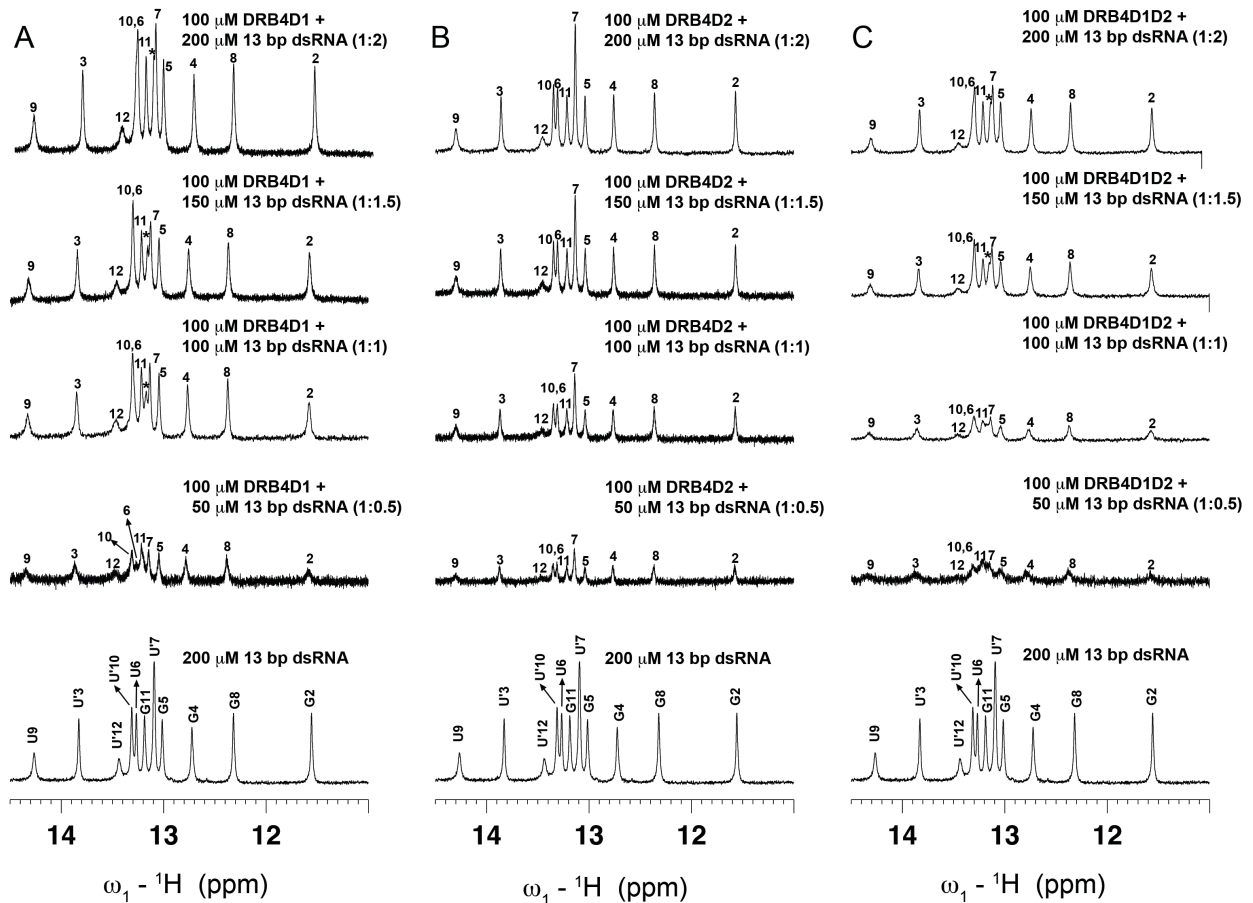
**Supplementary Figure S2.** Structural characterization of DRB4C. **(A)** Sedimentation velocity experiment showing absorbance scans and residuals as a function of radius represented for every 24 min (data collected at every 12 min). The bottom panel shows sedimentation coefficient distribution  $c(s)$ , which yielded 25.2 kDa molecular weight, suggesting a stable monomer. **(B)**  $^1\text{H}$ - $^{15}\text{N}$  TROSY-HSQC of DRB4C in presence of 6 M GuHCl. Narrow spectral dispersion in proton dimension and nearly identical  $^{15}\text{N}$  linewidths for all resonances strongly suggests denatured state.



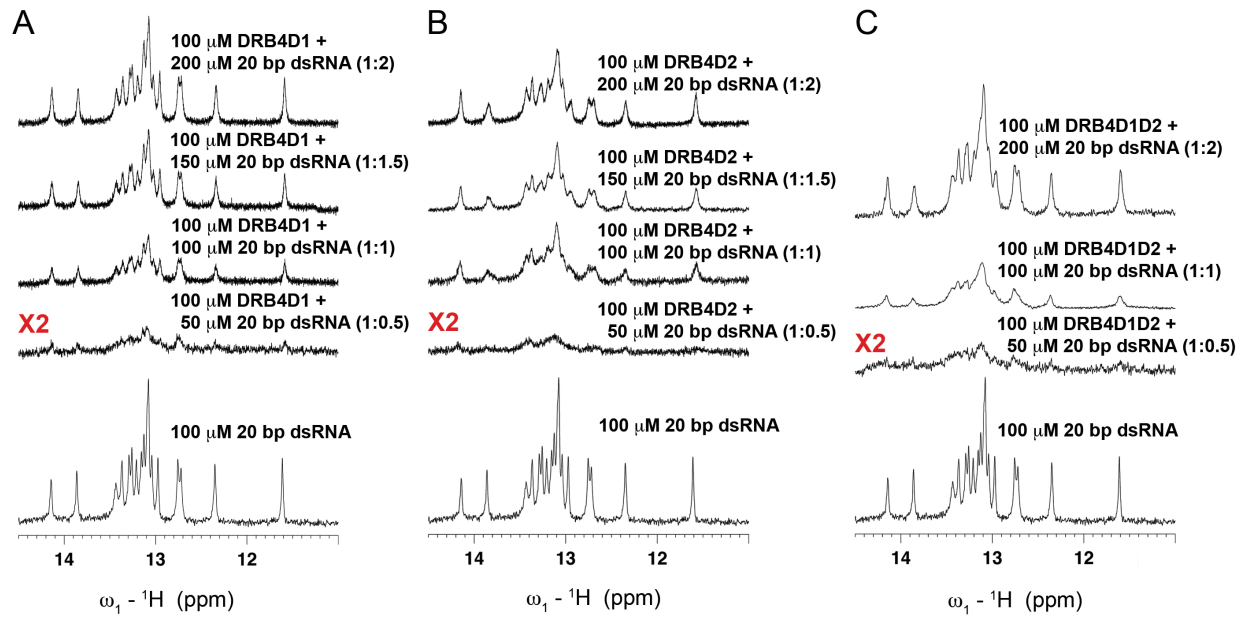
**Supplementary Figure S3.** Functional characterization of DRB4C. **(A)**  $^1\text{H}$ - $^{15}\text{N}$  TROSY-HSQC of DRB4C (red, 100  $\mu\text{M}$ ) in presence of  $\text{ZnCl}_2$  (blue, 1 mM). Broadening of a few resonances clearly indicate binding of  $\text{Zn}^{2+}$  with DRB4C. Residues that significantly broaden out ( $|I/I_0| < 0.2$ ) are: V262, T264, L265, A269, I273, K274, A279, C280, S282, W283, M284, T289, G292, E294, T295, S296, V299, V300, D301, E302, E304, K305, G311, T312, and G313. **(B)** ITC data of DRB4D1D2 with  $\text{ZnCl}_2$  yields a flat isotherm suggesting that DRB4D1D2 and  $\text{ZnCl}_2$  do not interact. **(C)** ITC derived thermodynamic analysis did not show binding between DRB4C and dsDNA.



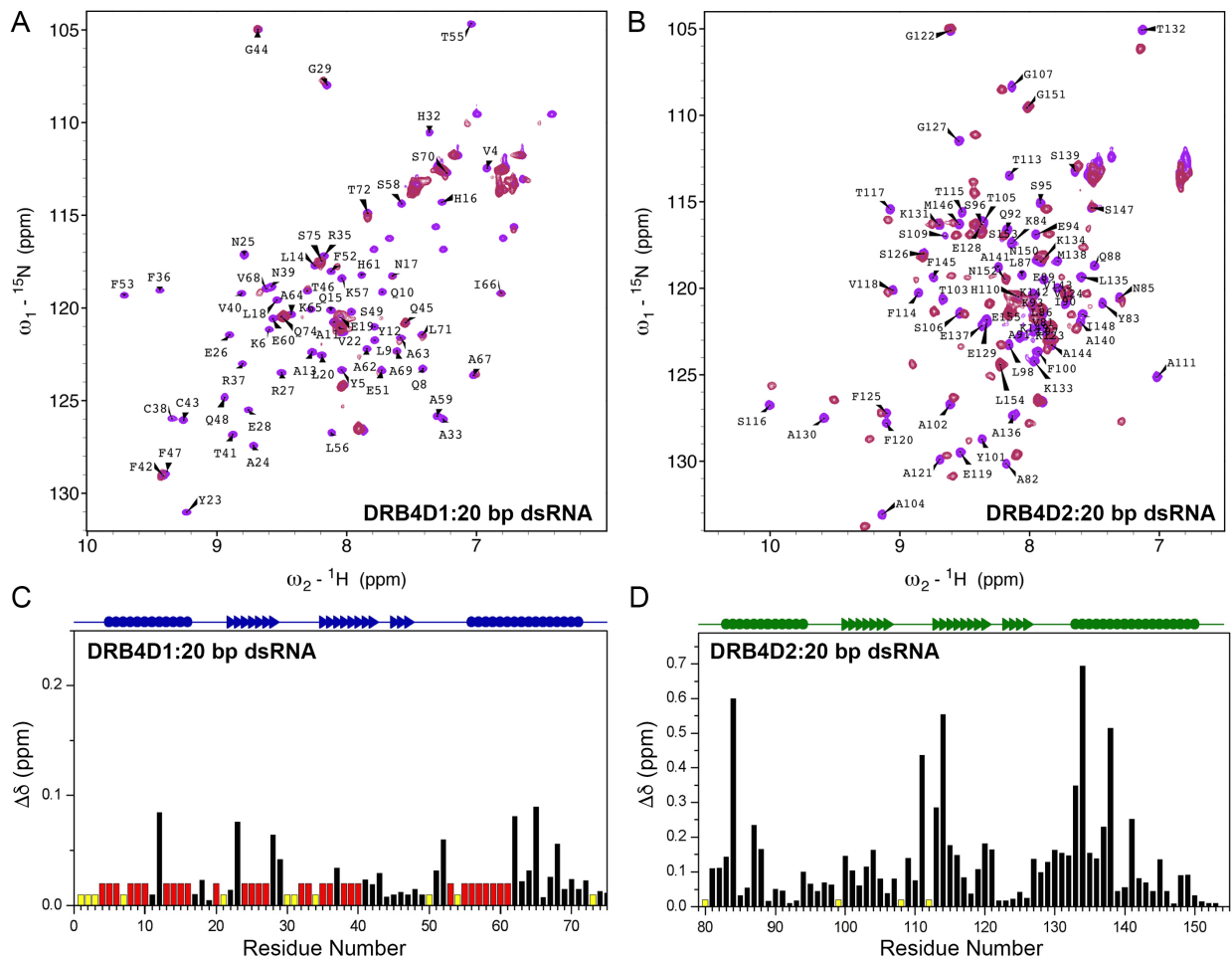
**Supplementary Figure S4.** Charge distribution and structure comparison of DRB4D1 and DRB4D2. Surface charges are represented for **(A)** DRB4D1 and **(B)** DRB4D2 at  $-5kT/e$  (red) to  $+5kT/e$  (blue). Contiguous positive charge is observed on alpha helical face of both dsRBDS. Structure overlay of DRB4D1 with HYL1D1 and **(C)** DRB4D2 with **(D)** HYL1D1 resulted in a backbone RMSD of 0.8 and 1.5 Å, respectively.



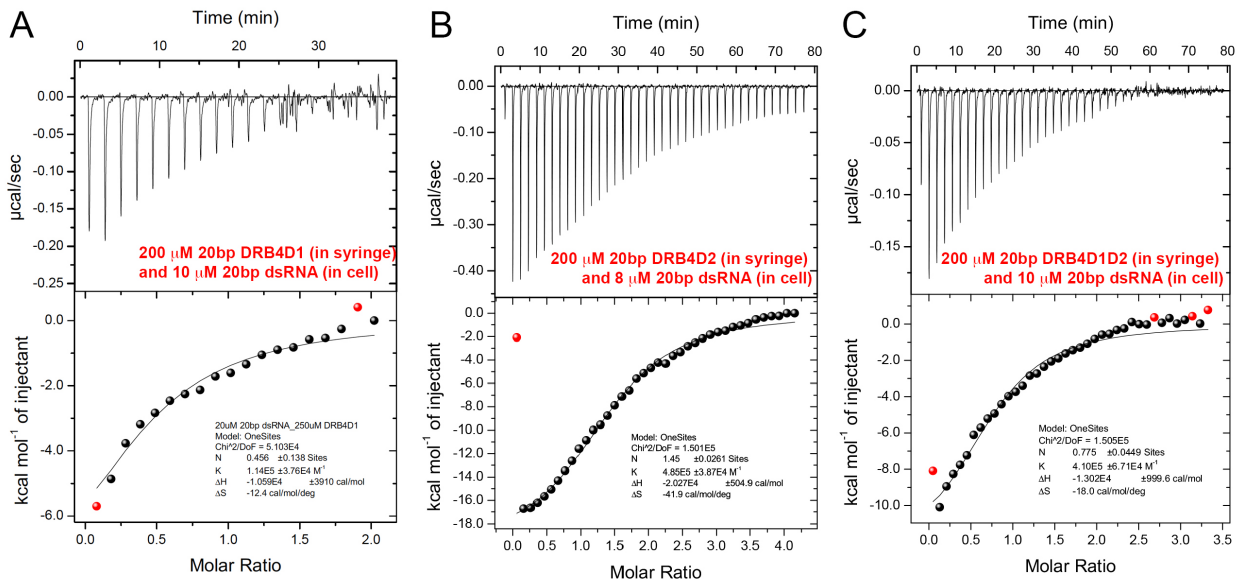
**Supplementary Figure S5.** 1D  ${}^1\text{H}$  NMR of 13 bp dsRNA representing the imino proton fingerprint region in free state and upon titration with **(A)** DRB4D1, **(B)** DRB4D2, and **(C)** DRB4D1D2. Assigned chemical shifts for the imino protons are annotated above each resonance. The minor shift for U'10 and U6 as well as the resonance annotated with an asterisk in **(A)** and **(C)**, features that are missing in **(B)**, are primarily due to the different local environment caused by different amino acids in the dsRNA binding region of dsRBD1 over dsRBD2. The dampened intensities for all resonances in the titration data of **(C)** are due to significantly reduced receiver gain during experimental conditions. Importantly, changes experienced by 13 bp dsRNA upon titration with DRB4D1 and DRB4D1D2 are identical suggesting that DRB4 dsRBD1 is the key dsRNA binding domain.



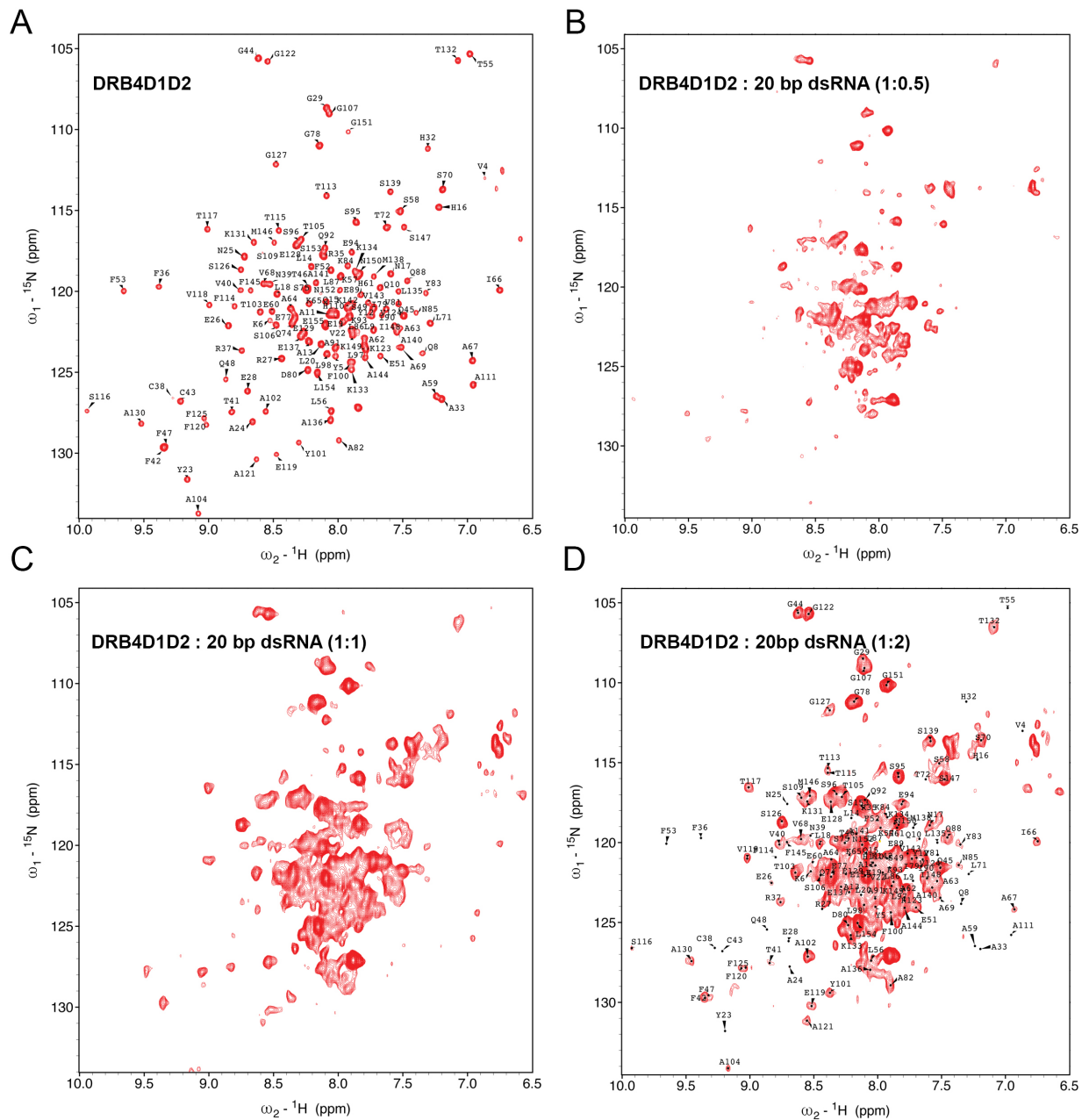
**Supplementary Figure S6.** The imino proton fingerprint region in the free and the bound state of 20 bp dsRNA upon titration with (A) DRB4D1, (B) DRB4D2, and (C) DRB4D1D2. At molar excess concentrations, the imino peaks appear better as they originate from the excess free RNA in the titration mixture. Due to the significant broadening of all imino protons at 1:0.5 molar ratio of protein:dsRNA, the peaks are represented with factor two enhancement. Contrary to the 13 bp dsRNA titration (Supplementary Fig S5), majority of the imino protons experience broadening at or below molar equivalence implying that DRB4 dsRBDs recognize longer dsRNA using a different binding mechanism. The free dsRNA spectrum (bottom spectrum in all panels) and all the data in (C) are comparatively better resolved as these were collected at a 700 MHz NMR spectrometer.



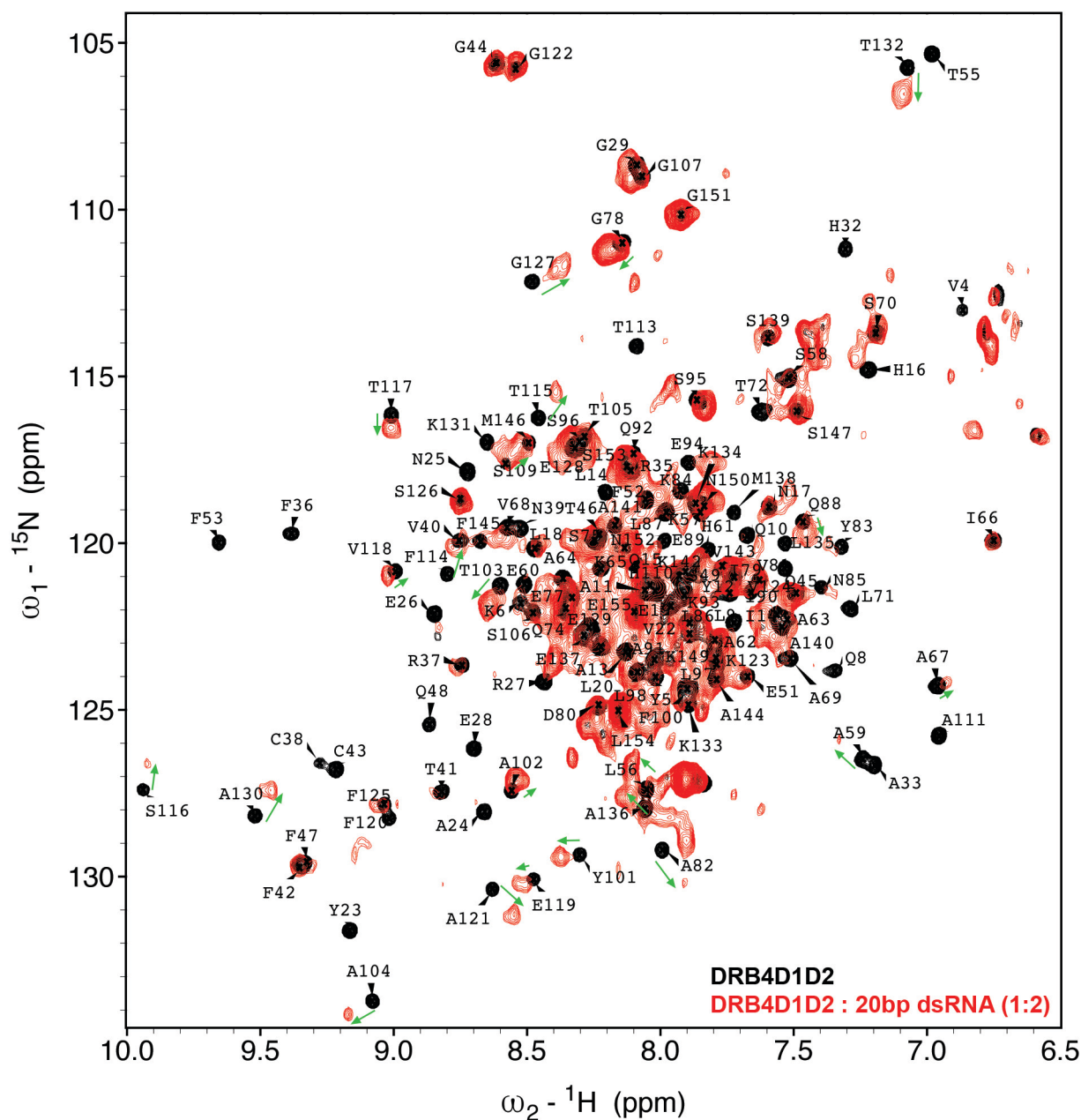
**Supplementary Figure S7.** Binding of 20 bp dsRNA with DRB4D1 and DRB4D2. **(A)**  $^1\text{H}$ - $^{15}\text{N}$  HSQC reveals severe broadening of resonances for DRB4D1 residues in the presence of 20 bp dsRNA. **(B)** Residues in DRB4D2 undergo chemical shift perturbations in the presence of 20 bp dsRNA. Cross peaks in purple and brown represent protein in the absence and presence of 20 bp dsRNA, respectively. **(C)** Normalized chemical shift deviations with 20 bp dsRNA show that almost all residues in DRB4D1 undergo broadening and artificially annotated with a flat 0.02 ppm  $\Delta\delta$  value (red), except for few residues in  $\beta 3$  and C-terminal of  $\alpha 2$ , which are present on the opposite side of dsRNA binding surface. **(D)** Bar graph shows that canonical dsRNA binding residues (in  $\alpha 1$ ,  $\beta 1$ - $\beta 2$  loop and  $\alpha 2$ ) of DRB4D2 take part in the binding with 20 bp dsRNA. Yellow bars in **(C)** and **(D)** represents unassigned/Proline residues and red bars are the residues which undergo broadening.



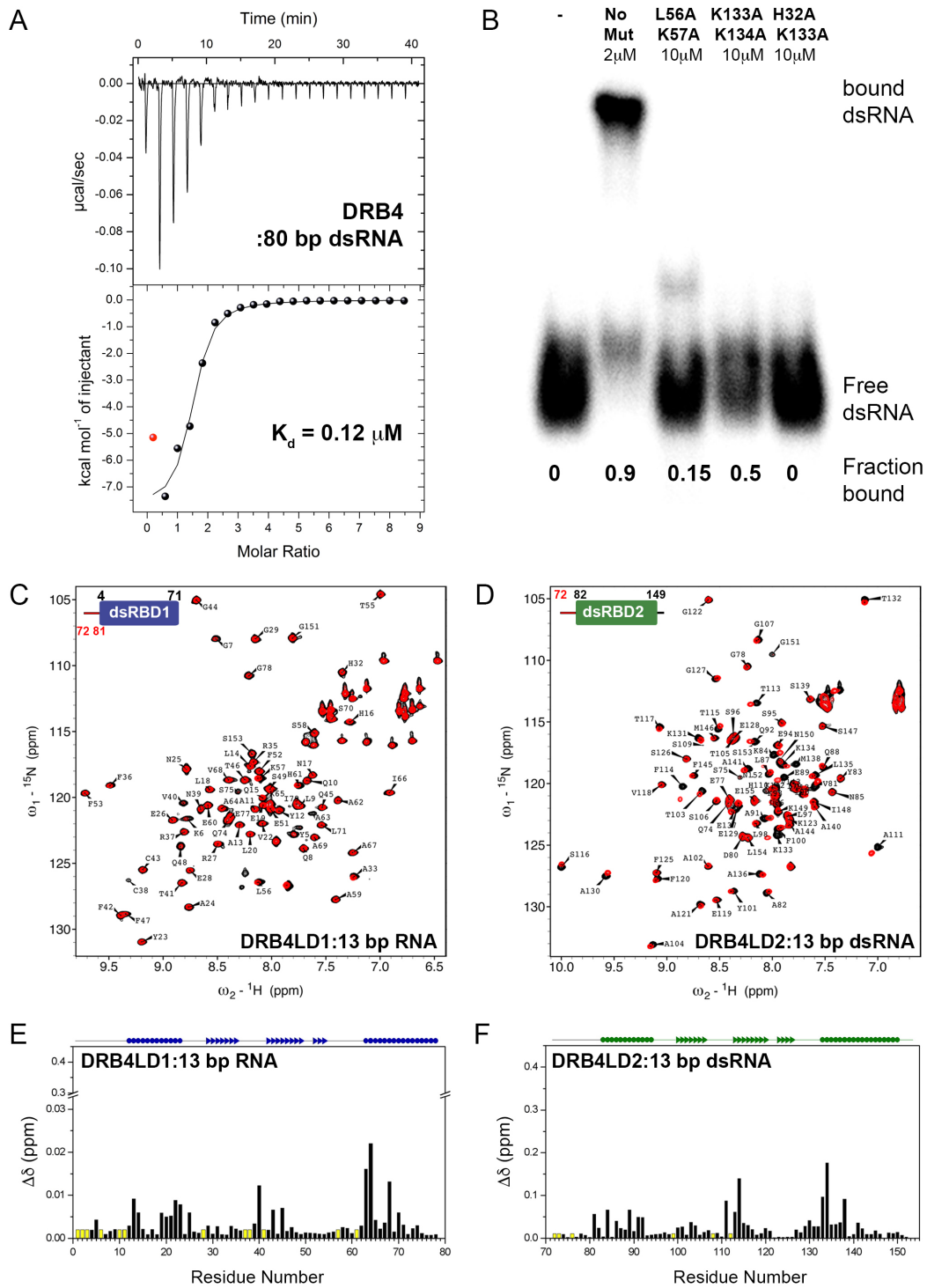
**Supplementary Figure S8.** ITC derived isotherm for the titration between 20 bp RNA with (A) DRB4D1, (B) DRB4D2, and (C) DRB4D1D2. These studies were performed with 20 bp dsRNA in cell and DRB4 domains in the syringe. Inset in each panel shows parameters derived during the fitting of the raw data which are also listed separately in Table S1C. The isotherm obtained for DRB4D2 is highly identical to Fig 3F suggesting that the DRB4D2:20 bp dsRNA binding mode is independent of the titrant. The fitted isotherm yielded a single-site average binding mode due to the availability of free excess dsRNA in the cell, in contrast to the two-site binding mode obtained for DRB4D1 and DRB4D1D2 earlier when the dsRNA from syringe was titrated with protein in the cell (Fig 3C and 5C).



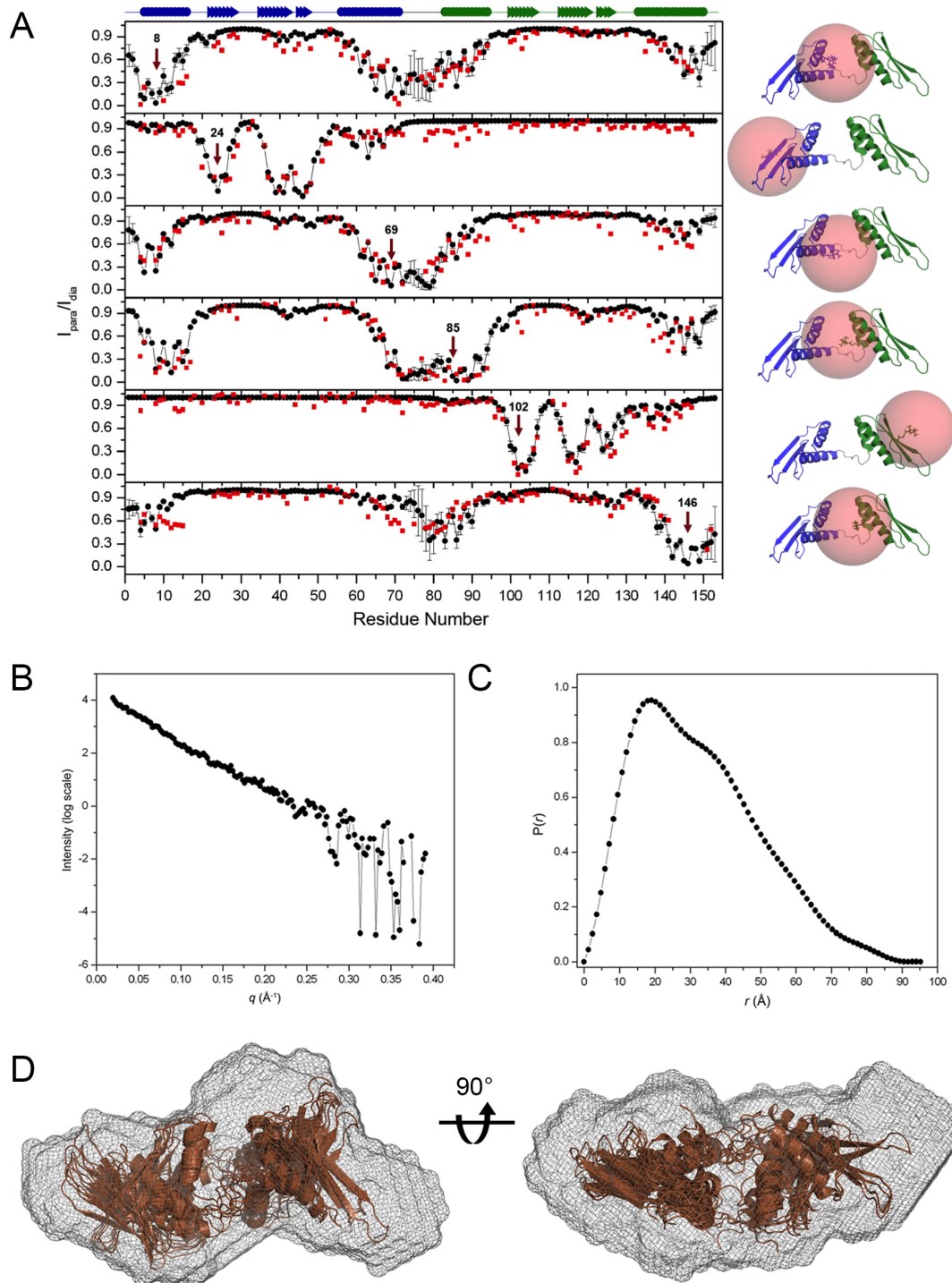
**Supplementary Figure S9.**  $^1\text{H}$ - $^{15}\text{N}$  HSQC of DRB4D1D2 upon titration with increasing concentration of 20 bp dsRNA (**A**) 100  $\mu\text{M}$  DRB4D1D2, (**B**) 100  $\mu\text{M}$  DRB4D1D2: 50  $\mu\text{M}$  20 bp dsRNA (1:0.5), (**C**) 100  $\mu\text{M}$  DRB4D1D2: 100  $\mu\text{M}$  20 bp dsRNA (1:1), and (**D**) 100  $\mu\text{M}$  DRB4D1D2: 200  $\mu\text{M}$  20 bp dsRNA (1:2). The broadening resonances are seen for the majority of DRB4D1D2 residues. Comparison of (**A**) and (**D**) reveals that resonances belonging to the dsRNA binding  $\alpha$ -helical face of dsRBD1 are broadened beyond detection. However, remaining peaks in dsRBD1, the linker and dsRBD2 experience lesser degree of broadening and are assignable. dsRNA binding residues of dsRBD2 could not be fully traced due to significant overlap in the central region.



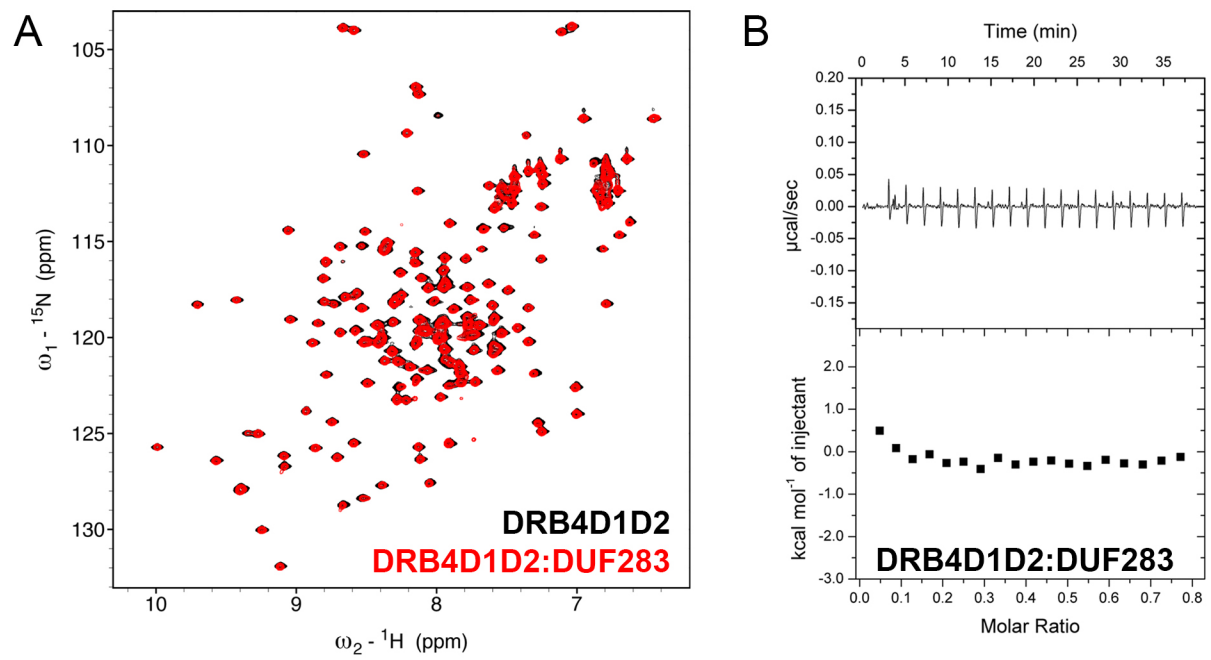
**Supplementary Figure S10.** Overlay of  $^1\text{H}$ - $^{15}\text{N}$  HSQC of DRB4D1D2 (black) and upon titration with 20 bp dsRNA (red). Green arrows show changes in the chemical shifts. Resonances arising from residues located on the  $\alpha$ -helical face of dsRBD1 show significant broadening (consistent with DRB4D1, Supplementary Fig S7A and Supplementary Fig S7C), whereas majority of the dsRBD2 residues predominantly exhibit chemical shift perturbations (consistent with DRB4D2, Supplementary Fig S7B and Supplementary Fig S7D) albeit with some broadening. The dsRBD2 also show relatively weaker perturbations as only  $\sim 30\%$  is able to bind to dsRNA (in corroboration with observation made in Fig. S6A). The dsRBDs in DRB4D1D2 retain the longer dsRNA recognition characteristics as exhibited by the individual domains. Collectively, it appears that the broadening exhibited by dsRBD1 is due to multiple bindings (upto four) as well as its ability to slide on long dsRNA whereas dsRBD2 makes transient contacts. As dsRBD2 cannot bind to the same dsRNA that is already occupied with dsRBD1, a complex macromolecular assembly formed by two molecules of dsRNA and DRB4D1D2 is probably causing broadening observed in the 1D NMR of imino protons of 20 bp dsRNA at an equimolar concentration (Supplementary Fig S6C).



**Supplementary Figure S11.** dsRNA binding studies of DRB4, DRB4LD1 and DRB4LD2. **(A)** Top panel shows the raw ITC titration data of DRB4 with 80 bp dsRNA. Enthalpy per mol<sup>-1</sup> of injection was integrated and plotted as a function of molar ratio of protein to dsRNA. The fit represents a  $K_d$  of  $0.12 \pm 0.04 \mu\text{M}$  with two molecules of DRB4 binding to a 80 bp dsRNA. **(B)** EMSA performed for 80 bp dsRNA with DRB4 and its double mutants. At five times higher concentration of DRB4, only 50% loss in affinity is observed for K133A/K134A double mutant (lane4), whereas, L56A/K57A (lane3) loses 85% of its binding ability, on the extreme H32A/K133A (lane 5) completely abrogates its binding with dsRNA. **(C)** Overlay of DRB4LD1 <sup>1</sup>H-<sup>15</sup>N HSQC in the absence (black) and presence (red) of 13 bp dsRNA. **(D)** Superposition of <sup>1</sup>H-<sup>15</sup>N HSQC of DRB4LD2 in the absence (black) and presence (red) of 13 bp dsRNA. **(E)** Normalized chemical shift perturbations along residue number signify loss of dsRNA binding ability of DRB4LD1. **(F)** Residue specific  $\Delta\delta$  plot reveals that extent of perturbations is significantly reduced in DRB4LD2 in comparison to DRB4D2. Yellow bars in **(E)** and **(F)** represent unassigned or proline residues.



**Supplementary Figure S12.** PRE and SAXS studies on DRB4D1D2. **(A)** Experimental PREs (red squares) were compared with back-calculated (black circles) PREs for MTSL spin label at Q8, A24, A69, N85, A102, M146 (from top to bottom) amino acid position and Q factors of 0.23, 0.14, 0.18, 0.20, 0.14, and 0.17, respectively, were obtained. Error on back-calculated  $I_{para}/I_{dia}$  was estimated using average distance from ten lowest energy solution structures. Location of the MTSL tag and its sphere of influence is shown in the right panel. **(B)** Raw SAXS data of DRB4D1D2. **(C)** Pair distribution function plot shows a skewed bell-shaped distribution revealing an elongated multi domain monodisperse molecule with presence of two domains and resulted in  $R_g$  25.8Å and  $D_{max}$  95.2Å. **(D)** Superposition of ten lowest energy PRE refined NMR structures (in cartoon representation) with averaged SAXS structure (in mesh representation). The average low-resolution structure illustrates that DRB4D1D2 adopts an extended conformation.



**Supplementary Figure S13.** Interaction studies of DRB4D1D2 with DCL4 DUF283. **(A)**  ${}^1\text{H}$ - ${}^{15}\text{N}$  HSQC overlay of DRB4D1D2 in the presence (red) and absence (black) of unlabeled DCL4 DUF283. **(B)** Binding isotherm of DRB4D1D2, titrated with DCL4 DUF283 did not result in significant heat enthalpy. Both experiments categorically rule out any possible interaction between DRB4D1D2 and DCL4 DUF283.

## Supplementary References

1. Chiliveri, S.C. and Deshmukh, M.V. (2015) Chemical shift assignments of DRB4 (1-153), a dsRNA binding protein in *A. thaliana* RNAi pathway. *Biomol. NMR Assign.*, **9**, 253–256.
2. Qin, H., Chen, F., Huan, X., Machida, S., Song, J. and Yuan, Y.A. (2010) Structure of the *Arabidopsis thaliana* DCL4 DUF283 domain reveals a noncanonical double-stranded RNA-binding fold for protein-protein interaction. *RNA*, **16**, 474–481.
3. Panchal, S.C., Bhavesh, N.S. and Hosur, R.V. (2001) Improved 3D triple resonance experiments, HNN and HN(C)N, for HN and <sup>15</sup>N sequential correlations in (<sup>13</sup>C, <sup>15</sup>N) labeled proteins: Application to unfolded proteins. *J. Biomol. NMR*, **20**, 135–147.
4. Chugh, J. and Hosur, R.V. (2008) Spectroscopic labeling of A, S/T in the <sup>1</sup>H-<sup>15</sup>N HSQC spectrum of uniformly (<sup>15</sup>N-<sup>13</sup>C) labeled proteins. *J. Magn. Reson.*, **194**, 289–294.
5. Shen, Y., Delaglio, F., Cornilescu, G. and Bax, A. (2009) TALOS+: A hybrid method for predicting protein backbone torsion angles from NMR chemical shifts. *J. Biomol. NMR*, **44**, 213–223.
6. Schwieters, C.D., Kuszewski, J.J., Tjandra, N. and Clore, G.M. (2003) The Xplor-NIH NMR molecular structure determination package. *J. Magn. Reson.*, **160**, 65–73.
7. Ottiger, M., Delaglio, F. and Bax, A. (1998) Measurement of J and dipolar couplings from simplified two-dimensional NMR spectra. *J. Magn. Reson.*, **131**, 373–378.
8. Battiste, J.L. and Wagner, G. (2000) Utilization of site-directed spin labeling and high-resolution heteronuclear nuclear magnetic resonance for global fold determination of large proteins with limited nuclear overhauser effect data. *Biochemistry*, **39**, 5355–5365.
9. Rumpel, S., Becker, S. and Zweckstetter, M. (2008) High-resolution structure determination of the CylR2 homodimer using paramagnetic relaxation enhancement and structure-based prediction of molecular alignment. *J. Biomol. NMR*, **40**, 1–13.
10. Hansen, D.F., Vallurupalli, P. and Kay, L.E. (2008) An improved <sup>15</sup>N relaxation dispersion experiment for the measurement of millisecond time-scale dynamics in proteins. *J. Phys. Chem. B*, **112**, 5898–5904.
11. Delaglio, F., Grzesiek, S., Vuister, G.W., Zhu, G., Pfeifer, J. and Bax, A. (1995) NMRPipe: A multi-dimensional spectral processing system based on UNIX pipes. *J. Biomol. NMR*, **6**, 277–293.
12. Goddard, T. and Kneller, D.G. SPARKY 3. *Univ. California, San Francisco*
13. Hammersley, A.P. (1997) FIT2D: An Introduction and Overview. *ESRF Intern. Rep.*
14. Konarev, P.V., Volkov, V.V., Sokolova, A.V., Koch, M.H.J. and Svergun, D.I. (2003) PRIMUS: A Windows PC-based system for small-angle scattering data analysis. *J. Appl. Crystallogr.*, **36**, 1277–1282.
15. Svergun, D.I. (1992) Determination of the regularization parameter in indirect-transform methods using perceptual criteria. *J. Appl. Crystallogr.*, **25**, 495–503.
16. Kozin, M.B. and Svergun, D.I. (2001) Automated matching of high- and low-resolution structural models. *J. Appl. Crystallogr.*, **34**, 33–41.
17. Volkov, V.V. and Svergun, D.I. (2003) Uniqueness of *ab initio* shape determination in small-angle scattering. *J. Appl. Crystallogr.*, **36**, 860–864.